Graphical Abstract

A Modified Step-Adaptive Perturb and Observe Control Algorithm for a Tracking-Integrated Micro-Concentrator Photovoltaic (WiT-CPV) System

Fernando Dávalos Hernández, Arturo Díaz-Ponce, Iván Trejo-Zúñiga, Rosa C. Anguiano Cota, Pedro M. Rodrigo, María A. Ceballos, Álvaro Valera-Albacete, Florencia Almonacid, Eduardo F. Fernández

Highlights

A Modified Step-Adaptive Perturb and Observe Control Algorithm for a Tracking-Integrated Micro-Concentrator Photovoltaic (WiT-CPV) System

Fernando Dávalos Hernández, Arturo Díaz-Ponce, Iván Trejo-Zúñiga, Rosa C. Anguiano Cota, Pedro M. Rodrigo, María A. Ceballos, Álvaro Valera-Albacete, Florencia Almonacid, Eduardo F. Fernández

- A step-adaptive P&O controller keeps the cell on the moving Petzval focal spot without an MPPT stage
- A dual-core ESP32 board with TMC2209 drivers and a 24-bit ADC provides synchronized I_{sc}/V_{oc} sensing and IoT telemetry
- 67.3% tracking efficiency (72.4 mW mean absolute power error) over a 6.3 h outdoor session
- A selected two-hour window reached 88.5% on-target sample occupancy
- Axis movement costs were estimated at 0.200 and 0.417 mJ per step

A Modified Step-Adaptive Perturb and Observe Control Algorithm for a Tracking-Integrated Micro-Concentrator Photovoltaic (WiT-CPV) System

Fernando Dávalos Hernández[a,*], Arturo Díaz-Ponce[b,c], Iván Trejo-Zúñiga[c], Rosa C. Anguiano Cota[d], Pedro M. Rodrigo[a], María A. Ceballos[e], Álvaro Valera-Albacete[e], Florencia Almonacid[e], Eduardo F. Fernández[e]

[a] *Universidad Panamericana, Facultad de Ingeniería, Jose María Escrivá de Balaguer 101, Villas Bonaterra, Aguascalientes, 20296, Aguascalientes, México*
[b] *SECIHTI – Centro de Investigaciones en Óptica, A.C., Unidad Aguascalientes, Prol. Constitución 607, Fracc. Reserva Loma Bonita, Aguascalientes, 20200, Aguascalientes, México*
[c] *Laboratory of Energy Innovation and Intelligent and Sustainable Agriculture (LEIISA), Universidad Tecnológica de San Juan del Río, Av La Palma No 125 Vista Hermosa, San Juan del Río, 76800, Querétaro, México*
[d] *Facultad de Ingeniería, Universidad Autónoma de Baja California (UABC), Blvd. Benito Juárez SN, Mexicali, 21280, Baja California, México*
[e] *Advances in Photovoltaic Technology (AdPVTech), CEACTEMA, University of Jaén, Las Lagunillas Campus, Jaén, 23071, Jaén, Spain*

Abstract

Tracking-integrated concentrating photovoltaic (TI-CPV) modules transfer part or all of the required solar-tracking motion inside the module itself, replacing large external structures with compact internal actuation. While this architecture reduces mechanical complexity, it introduces a distinct control problem: the receiver must follow a curved, optically-defined focal trajectory (the Petzval surface) rather than the Sun's apparent position, within a limited actuation range and without the benefit of a conventional electronic MPPT stage. This work presents the control architecture developed for a previously reported wide-acceptance-angle tracking-integrated micro-concentrator photovoltaic (WiT-CPV) prototype, focusing on the algorithm and hardware required to keep the multi-junction solar cell aligned with the moving focal spot of the primary biconvex aspheric lens. A modified, step-adaptive Perturb and Observe (P&O) strategy is proposed, using short-circuit current (I_{sc}) sampling as a direct proxy for optical alignment, avoiding the additional circuit complexity of an active MPPT converter during this proof-of-concept validation stage. The algorithm combines four operating regimes, a noise-filtering static-hold, a fine-convergence stage near the power peak, a cloud-transient shielding mode, and a search-reinitialization mode, to suppress mechanical jitter or hunting while remaining responsive to fast irradiance transients. The controller is implemented on a custom dual-core ESP32-based board with TMC2209 stepper drivers, sensorless StallGuard4 homing, and a 24-bit delta-sigma ADC for synchronized I_{sc}/V_{oc} sensing, integrated with an IoT telemetry layer for real-time logging. The proposed algorithm is experimentally evaluated on the WiT-CPV prototype, first in the laboratory under a calibrated solar simulator (1000 W/m^2, AM1.5G) and then over a full-day outdoor session on 21 September 2025, using a set of tracking-quality metrics including tracking efficiency (η_{tr}), mean absolute error in power, disturbance-recovery time (t_{95}), accumulated actuator microsteps, and the parasitic consumption ratio (PCR). Over the outdoor session the modified P&O strategy achieved a tracking efficiency of 67.3% with a mean absolute power error of

72.4 mW, and the irradiance recovered to 95% of its pre-event baseline in 124–180 s following the deepest cloud transients (87% depth), with the controller re-acquiring the power peak within the same time frame; the parasitic consumption ratio will be reported in a follow-up session once the board-consumption logging is available. These findings demonstrate that a lightweight, current-based control strategy can provide robust and energy-efficient focal alignment for micro-tracking CPV systems, supporting their scalability toward low-power, low-cost agrivoltaic and building-integrated deployments. An additional outdoor evaluation on 30 October 2026 focuses on the explicitly selected 12:00–14:00 window, in which 88.5% of the logged samples satisfied an on-target criterion of at least 80% of the window peak short-circuit current under illumination. This sample-occupancy metric is distinct from energy-based tracking efficiency. Bench measurements of axis power and travel time also provide a first-order movement-energy model, with costs of approximately 0.200 and 0.417 mJ per commanded step for the X and Y axes, respectively. Applied to the sampled axis travel, this model estimates 0.0663 Wh of movement energy in the selected window; unobserved travel, standby and controller consumption remain outside this estimate.

Keywords: Micro-tracking, Tracking-integrated CPV, Perturb and Observe, Focal-point tracking, Embedded control system, Proof-of-concept validation

1. Introduction

The efficient utilization of solar radiation through photovoltaic systems depends not only on the available energy but also on the geometric conditions under which it impinges on the receiving surface. The incidence angle, determined by the Sun's position and the orientation of the device, directly influences the radiation captured and, consequently, the energy yield of the system [1],[2]. Due to the apparent motion of the Sun, these conditions vary throughout the day and year, so a fixed orientation cannot maintain optimal collection conditions during the entire operating period. To compensate for this variation, different solar tracking solutions have been developed, ranging from passive mechanisms to active one- and two-axis systems integrating electromechanical actuators, sensors, embedded controllers, and solar position models [3, 4, 2, 5, 6]. Although they differ in configuration, accuracy, and complexity, these solutions aim to maintain a favorable orientation of the module or collector with respect to the solar direction. Experimental comparisons between fixed modules and dual-axis tracking systems confirm that reorientation can significantly increase the captured radiation [1]. Tracking performance is not determined solely by positioning accuracy. Sensor resolution, actuation frequency, mechanical characteristics, and the energy required for corrections also condition system operation. Active trackers may employ open-loop strategies based on solar position calculations, closed-loop strategies using feedback signals, or hybrid approaches combining both [7]. Positioning control may coexist with maximum power point tracking (MPPT) techniques, although they serve different purposes: solar tracking modifies the geometric conditions of radiation capture, while MPPT adjusts the electrical operating point of the photovoltaic device [8]. These considerations become more restrictive when optical concentration is introduced. Concentrating photovoltaic (CPV) systems employ optical elements to focus radiation onto receivers with active

*Corresponding author. Email: fdavalos@up.edu.mx

areas smaller than the concentrator aperture, enabling the use of high-efficiency devices such as multi-junction cells [9, 10]. Their performance depends on parameters such as concentration ratio, acceptance angle, optical efficiency, and irradiance distribution on the receiver [10, 11]. A deviation in the incidence direction may not only reduce the intercepted energy but also displace the concentrated irradiance distribution relative to the active cell area. Consequently, tracking accuracy is closely linked to the optical performance of the concentrator and the ability to maintain spatial correspondence between optics and receiver [12]. In conventional CPV configurations, this correspondence is maintained by reorienting the entire concentrator along the solar trajectory. This procedure requires simultaneous displacement of the structure, optical elements, and receiver, with corresponding demands in actuation, mechanical support, and precision. These requirements become more critical as the dimensions and mass of the system increase, driving the search for solutions capable of preserving optical alignment through smaller-scale displacements. Concentrating photovoltaic systems with integrated tracking (TI-CPV) transfer part or all of the required motion into the module itself [11]. Instead of reorienting the entire concentrator, these architectures compensate for focal region displacement through relative movements between optical elements and the photovoltaic receiver. Ito et al. developed a CPV module based on an array of biconvex aspheric lenses and three-dimensional displacement of photovoltaic cells [13]. Askins et al. investigated a microconcentration configuration with planar tracking designed to exploit both direct and diffuse radiation components [14]. Other architectures have explored different combinations of optics and internal motion, demonstrating the potential of microtracking to reduce large-scale displacements associated with conventional CPV systems [15, 11]. Nevertheless, transferring tracking into the module does not eliminate the positioning problem. TI-CPV architectures rely on the motion of the receiver, optical elements, or both, so the available angular range, module thickness, and mechanical requirements depend on the adopted configuration [11]. The feasibility of this approach has also been experimentally demonstrated in systems intended for building integration, where external tracking structures face greater restrictions [16]. In these systems, tracking capability no longer depends exclusively on global module orientation but is conditioned by the relationship between internal motion and optical behavior. This distinction is particularly relevant from a control perspective. When the receiver or optical elements are displaced internally, the required position is determined by the spatial evolution of the focal region and by the physical constraints of the mechanism. Thus, knowledge of the Sun's apparent position alone does not define the motion to be performed inside the module: optical geometry dictates the trajectory to be followed, while kinematics and actuation limits establish the achievable positions. Microtracking therefore constitutes a coupled problem in which optical behavior and mechanical response must be jointly considered to maintain correspondence between the focal region and the receiver [13, 11]. Despite advances in TI-CPV architectures, this coupling imposes control requirements distinct from those of conventional solar trackers. Internal motion must be executed within a limited operating space, with precision compatible with focal characteristics and considering the kinematic constraints of the mechanism. Control strategies must therefore respond not only to solar position variation but also to the trajectory imposed by the optical system and the dynamics of the positioning mechanism. The integration of these aspects turns microtracking into an optomechatronic problem, where optics, mechanics, electronics, and control jointly determine receiver positioning.

The wide-acceptance-angle tracking-integrated micro-concentrator photovoltaic (WiT-CPV) prototype addressed in this work, comprising the biconvex aspheric primary optics, the dual-axis actuated stage with azimuthal cell rotation, and a first-generation electronic controller implementing a basic perturb and observe routine, has been previously reported in detail [17]. That

study presented the optical and mechanical design of the prototype together with the laboratory characterization of its subsystems, and deferred the quantitative evaluation of its tracking performance to a subsequent study. This article provides that follow-up contribution: it develops the step-adaptive control algorithm and the revised embedded controller described below, and reports the first full-day outdoor performance evaluation of the prototype.

Nomenclature

Symbol	Description	Unit
A, B, C	Coefficients of the clear-sky irradiance model $G_{\mathrm{cs}} = A\,e^{-B\,\mathrm{AM}} + C$	–
$C_{\max}$	Local maximum power baseline detected during search convergence	W
E	Harvested electrical energy	Wh
$E_{\mathrm{parasitic}}$	Board and motor energy consumption	Wh
E_{move}	Estimated motor energy during commanded motion	Wh
FF	Cell fill factor under concentrated standard test conditions	–
G, G_{POA}	Global irradiance (plane of array)	W m^{-2}
G_{base}, $G_{\min}$	Pre-event baseline and minimum irradiance during a cloud transient	W m^{-2}
G_{cs}	Clear-sky irradiance model	W m^{-2}
H	Plane-of-array irradiation	kWh m^{-2}
H_s	Solar hour	h
I_{sc}	Short-circuit current	A
$\Delta I_{sc,k}$	Short-circuit current variation between iterations k and $k-1$	A
MAE	Mean absolute power error	mW
N	Number of sampled log intervals	–
N_{cycle}	Local search cycle index	–
P_{CPV}	Electrical power generated by the multi-junction solar cell	W
P_{ref}	Reference power ceiling under ideal focal alignment	W
P_{95}	95% recovery threshold of the reference power ceiling	W
PCR	Parasitic consumption ratio	%
$R_{\mathrm{opt,max}}$	Maximum optical responsivity at perfect focus	A m^2 W^{-1}
S_{el}, S_{az}, S_{tot}	Cumulative microstep travel along the zenithal, azimuthal, and both axes	usteps
S_X, S_Y	Absolute commanded step travel used in the axis-energy model	steps
f_{on}	Fraction of samples satisfying the illuminated on-target criterion	%
q_X, q_Y	Estimated movement-energy cost per commanded axis step	J step^{-1}
T	Evaluation window duration	h
V_{oc}	Open-circuit voltage	V
X_k, Y_k	Motor step coordinates along the zenithal and azimuthal axes	usteps
t_{95}	Disturbance recovery time (power)	s
t_{95}^{G}	Disturbance recovery time (irradiance)	s
e_k	Adaptive displacement step size at iteration k	usteps
$e_{\min}$, $e_{\max}$	Minimum and maximum bounds of the adaptive step size	usteps
α_s	Solar zenith angle	$^\circ$
γ_s	Solar azimuth angle	$^\circ$
δ_{peak}	Proximity band around the local power peak	%
η_{tr}	Tracking efficiency	%
$\mathrm{TH}_{\mathrm{small}}$, $\mathrm{TH}_{\mathrm{abrupt}}$, $\mathrm{TH}_{\mathrm{reset}}$	Noise, cloud-transient, and search-reinitialization thresholds	A, A, W m^{-2}

Acronyms

Acronym	Full form
ADC	Analog-to-digital converter
AM	Air mass
CPV	Concentrator photovoltaic
HCPV	High-concentration photovoltaic
IoT	Internet of things
MJSC	Multi-junction solar cell
MPPT	Maximum power point tracking
NVS	Non-volatile storage
P&O	Perturb and Observe
PSRAM	Pseudostatic random-access memory
TI-CPV	Tracking-integrated CPV
WiT-CPV	Wide-acceptance-angle tracking-integrated micro-concentrator photovoltaic

2. System Dynamics and Mechanical Model

2.1. Petzval Surface Trajectory and Kinematic Coupling

2.2. Actuation Constraints and State Space Limits

3. Proposed Controller

The WiT-CPV system control architecture is engineered to dynamically maintain the multi-junction solar cell (MJSC) positioned at the moving focal spot of the primary biconvex aspheric lens. Active motion control is implemented along the zenithal (X) and azimuthal (Y) axes using low-power linear actuation, while Z-axis tracking naturally follows the Petzval surface curvature through guided mechanical tracks. It is worth noting that traditional electronic Maximum Power Point Tracking (MPPT) converters were intentionally omitted from the embedded controller architecture. Because the primary control objective of the WiT-CPV system is physical focal alignment (positioning the cell at the Petzval focal spot), short-circuit current (I_{sc}) provides a direct, highly sensitive, and monotonic metric of concentrated optical alignment. Implementing an active DC-DC MPPT converter would introduce additional circuit complexity, weight, and dynamic switching losses. Instead, the proposed system employs periodic low-frequency I_{sc}/V_{oc} sampling via MOSFET Q_1, maintaining ultra-low parasitic power consumption while enabling accurate estimation of generated electrical power through the cell Fill Factor (FF).

3.1. Modified Step-Adaptive P&O Control Algorithm

To overcome the susceptibility of standard Perturb and Observe (P&O) algorithms to continuous mechanical jitter (hunting) and rapid overcast transients, a modified step-adaptive P&O strategy with noise suppression thresholds was implemented as a refinement of the basic P&O routine first deployed in the prototype [17].

The control core relies on short-circuit current (I_{sc}) sampling as the primary feedback metric for optical alignment. Let $I_{sc,k}$ represent the short-circuit current measured at iteration step k, and let $\Delta I_{sc,k} = |I_{sc,k} - I_{sc,k-1}|$ define the current magnitude variation. From these quantities, the

controller selects one of four operating regimes at each iteration and computes the corresponding adaptive displacement step size e_k.

Under steady irradiance, the algorithm remains in a static-hold regime that acts as a noise filter: if the current variation stays below the sensor noise floor $\mathrm{TH}_{\mathrm{small}}$, displacement is suspended ($e_k = 0$), which prevents the mechanical wear and parasitic energy loss associated with continuous hunting. When the sampled current approaches the local maximum within a tolerance proximity band (δ_{peak}, e.g., 1.5%), the algorithm enters the near-peak fine-convergence regime, in which the step size attenuates inversely with the local cycle index N_{cycle}:

$$e_k = \max\left(\frac{e_{\min}}{N_{\mathrm{cycle}} + 1},\, e_{\min}\right) \quad \text{if } I_{sc,k} \geq I_{sc,\max}(1 - \delta_{\mathrm{peak}}) \tag{1}$$

Fast illumination drops caused by passing cloud cover are identified when $\Delta I_{sc,k} > \mathrm{TH}_{\mathrm{abrupt}}$; to prevent off-focus drift during such temporary shadows, the cloud-transient shielding regime attenuates the step size as $e_k = \max(0.6 \cdot e_{k-1},\, e_{\min})$. Finally, if the global irradiance changes by more than $\mathrm{TH}_{\mathrm{reset}}$, indicating sky recovery or a significant solar drift, the search re-initialization regime resets the step size to its upper limit $e_{\max}$.

To decouple cross-axis mechanical coupling, the tracking loop alternates search cycles sequentially between the X (Zenith) and Y (Azimuth) axes every $N_{\mathrm{cycle,max}} = 3$ steps.

3.2. Controller Board Architecture and Hardware Design

The custom electronic control board is a revision of the first-generation design reported in [17], now built around a 32-bit dual-core ESP32 microcontroller and integrating motion control, high-resolution analog signal conditioning, and wireless IoT logging. The full system topology is depicted in Figure 1.

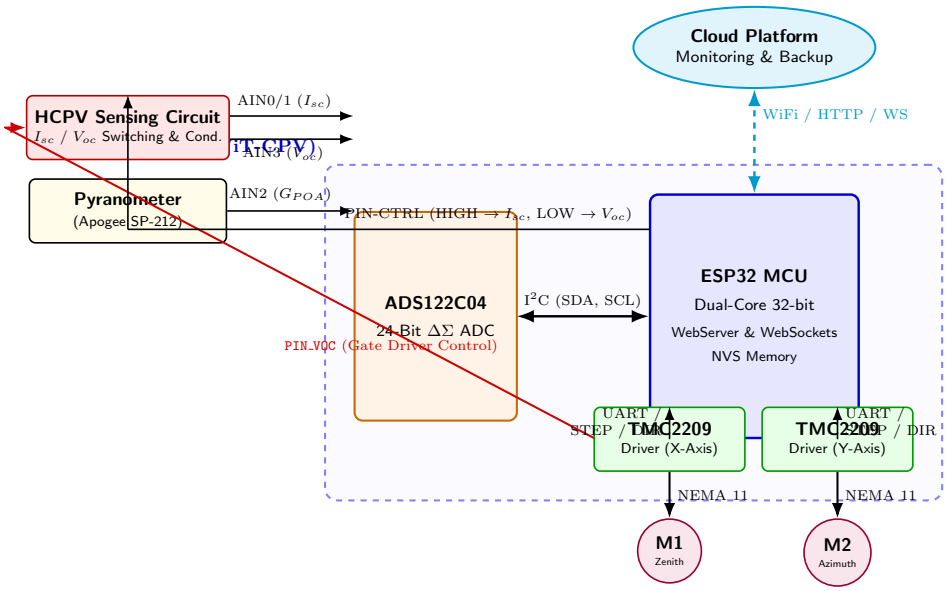


Figure 1: Top-level system architecture of the WiT-CPV controller board, displaying actuation, sensing conditioning, and IoT cloud communication pathways.

The ESP32 MCU manages both motion generation and network protocols. To ensure system recovery after power interruptions, motor step coordinates (X_k, Y_k) are saved to Non-Volatile Storage (NVS) using the `Preferences` library whenever displacements exceed 1000 microsteps, while real-time diagnostic logs are maintained locally in a 2 MB PSRAM circular buffer. Motion is delivered through two TMC2209 stepper motor drivers, which command the NEMA 11 linear actuators (M1 for Zenith, M2 for Azimuth) via hardware UART and Step/Dir interfaces; the drivers are configured for $1/8$ microstepping. At system initialization, sensorless homing is performed using StallGuard4 technology, which detects endstops through back-EMF monitoring, eliminating the need for physical limit switches.

The conversion of analog signals is handled by a 24-bit delta-sigma ADC (ADS122C04) interfaced via an I^2C bus. An Apogee SP-212 pyranometer is connected to the AIN2 input to sample the global irradiance of the plane-of-array (G_{POA}). The dedicated HCPV cell conditioning and switching circuitry, detailed in Figure 2, is driven by a control line (`PIN_VOC` / `PIN-CTRL`) from ESP32 that activates a MIC5019 high-side gate driver, which in turn controls an N-channel MOSFET Q_1 (DMN62D0UW-7). When Q_1 is saturated (HIGH state), the cell short-circuit current (I_{sc}) passes through a 75 mΩ shunt resistor, is amplified by an AD8418 current-sense amplifier, and is fed to ADC channels AIN0/AIN1. When Q_1 is opened (LOW state), the open-circuit voltage (V_{oc}) is instead sampled at channel AIN3 through a 10 kΩ/10 kΩ precision voltage divider, allowing the two electrical quantities to be measured sequentially with the same acquisition chain.

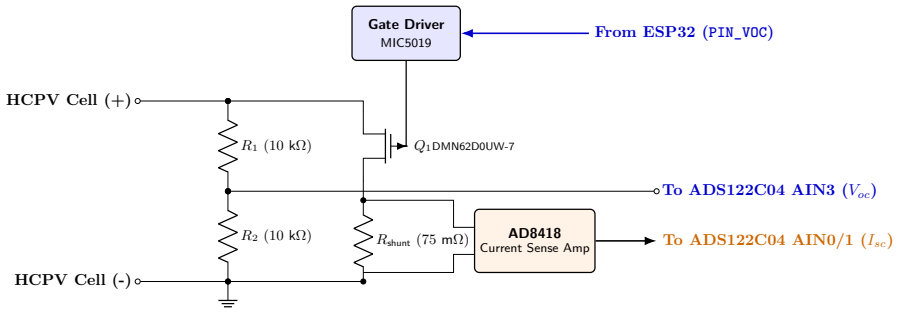


Figure 2: Schematic of the HCPV cell sensing and switching circuit for I_{sc} and V_{oc} acquisition using the MIC5019 gate driver, DMN62D0UW-7 MOSFET Q_1, 75 mΩ shunt, and AD8418 amplifier.

Finally, an integrated HTTP WebServer and WebSocket service (port 81) enables full-duplex live streaming of electrical parameters (I_{sc}, V_{oc}), solar irradiance (G_{POA}), motor coordinates, and control states to a cloud platform, providing continuous monitoring and data backup for the prototype.

The October 2026 evaluation uses the second PCB revision (V2), whose photocurrent shunt is 260 mΩ, rather than the 75 mΩ shunt shown for the earlier revision in Fig. 2. Its log channels are kept distinct: `C` denotes photocurrent and `P` denotes pyranometer irradiance. The October figures use the V2 shunt calibration and a pyranometer conversion divisor of 0.2; the older shunt value must not be applied to this record.

3.3. Proposed Hybrid Control Model (Future Work)

To eliminate search delays during heavy cloud cover, a dual-layer hybrid tracking framework is planned as a future development, combining open-loop astronomical positioning with closed-

loop optical optimization. In a first stage of coarse astronomical alignment, the system computes the theoretical solar vector (α_s, zenith; γ_s, azimuth) based on geographic location, date, and local solar time (H_s), executing rapid motor steps to target the deterministic focal position. Once the receiver is placed within the focal region, a second stage of closed-loop fine alignment takes over: the modified P&O routine activates to perform sub-millimetric adjustments, compensating for structural tolerances, module tilt errors, and mounting misalignment that the astronomical model alone cannot resolve.

4. Results and Discussion

4.1. Experimental Testbench Setup

Validation of the WiT-CPV prototype was conducted under controlled laboratory conditions using an Oriel LCS-100 continuous solar simulator, the same instrument used for the laboratory characterization of the prototype reported in [17], calibrated to standard operating conditions (1000 W/m^2, AM1.5G, 25°C). The physical movement range of the dual-axis stage was verified to cover ±30° along the zenithal axis and ±40° along the azimuthal axis with single-axis cell rotation.

4.2. Tracking Quality Evaluation

The evaluation quantifies how effectively the modified P&O algorithm maintains the multi-junction solar cell at the optimal focal point generated by the concentrating lens under varying solar position and irradiance conditions. The experimental indicators are organized in three complementary groups: the energy harvesting of the cell and its normalization against the available irradiation, the tracking quality with respect to the ideal focal power ceiling, and the mechanical activity together with the parasitic overhead incurred by the search process.

4.2.1. Energy Harvesting Metrics

The instantaneous electric power $P_{\mathrm{CPV}}(t)$ generated by the HCPV cell is modeled considering the measured short-circuit current $I_{sc}(t)$, open-circuit voltage $V_{oc}(t)$, and the cell Fill Factor ($FF \approx 0.82$), as characterized under concentrated standard test conditions:

$$P_{\mathrm{CPV}}(t) = I_{sc}(t) \cdot V_{oc}(t) \cdot FF \tag{2}$$

The total generated electrical energy E is subsequently calculated by integrating $P_{\mathrm{CPV}}(t)$ over the operation interval T:

$$E = \int_0^T I_{sc}(t) \cdot V_{oc}(t) \cdot FF \, dt \tag{3}$$

The available global solar irradiation (H) over a test period T are computed as:

$$H = \int_0^T G_{POA}(t) \, dt \tag{4}$$

where $G_{POA}(t)$ is the plane-of-array global irradiance measured by the on-board pyranometer. The normalized energy performance ($E_{1\mathrm{kWh/m^2}}$) assesses how effectively the system captures energy per unit of available solar irradiation:

$$E_{1\mathrm{kWh/m^2}} = \frac{E}{H} \quad \left[\mathrm{kWh/(kWh/m^2)}\right] \tag{5}$$

4.2.2. Tracking Quality Metrics

The reference power ceiling $P_{\mathrm{ref}}(t)$ defines the theoretical limit of the harvested power under ideal focal alignment. It is derived from the maximum optical responsivity of the concentrating optics, $R_{\mathrm{opt,max}} = \max(I_{sc}(t)/G_{\mathrm{POA}}(t))$, evaluated while the cell remains at the focal point:

$$P_{\mathrm{ref}}(t) = R_{\mathrm{opt,max}} \cdot G_{\mathrm{POA}}(t) \cdot V_{oc}(t) \cdot FF \tag{6}$$

Tracking accuracy then measures how closely the active controller maintains the harvested power at this ceiling. The tracking efficiency (η_{tr}) quantifies the proportion of the reference ceiling captured by the tracking loop over the experiment duration T, and the mean absolute error (MAE) evaluates the average deviation between the reference and the harvested power:

$$\eta_{\mathrm{tr}} = \frac{\int_0^T P_{\mathrm{CPV}}(t)\,dt}{\int_0^T P_{\mathrm{ref}}(t)\,dt} \times 100\% \tag{7}$$

$$\mathrm{MAE} = \frac{1}{N}\sum_{k=1}^{N}\left|P_{\mathrm{ref},k} - P_{\mathrm{CPV},k}\right| \tag{8}$$

where N is the total number of sampled log intervals, and $P_{\mathrm{ref},k}$ is the local maximum power baseline detected during search convergence ($C_{\max}$).

For the October evaluation, a separate on-target sample fraction is defined directly from the logged photocurrent:

$$f_{\mathrm{on}} = \frac{100\%}{N}\sum_{k=1}^{N}\mathbf{1}\left[I_{sc,k} \geq 0.8 I_{sc,\max}^{(W)} \ \wedge \ G_{\mathrm{POA},k} > 50\ \mathrm{W\,m^{-2}}\right], \tag{9}$$

where $I_{sc,\max}^{(W)}$ is the maximum current within the explicitly specified evaluation window W, and the denominator includes all N samples in that window. This is a current-threshold occupancy measure, not an angular-error measurement, optical conversion efficiency, or the energy-based η_{tr}. It is not normalized against irradiance beyond the illumination gate; changing irradiance can therefore affect it. With approximately uniform sampling it approximates a time fraction, but the reported value is calculated by sample count. Changing the window also changes its peak reference, so percentages from different windows are not directly interchangeable.

4.2.3. Disturbance Recovery Metrics

System responsiveness following sudden solar position re-alignment or cloud transients is evaluated through the recovery time t_{95}, defined as the time interval required for the generated power to recover to the threshold $P_{95} = 0.95 \cdot P_{\mathrm{ref}}$:

$$t_{95} = t\left(P_{\mathrm{CPV}} \geq 0.95 \cdot P_{\mathrm{ref}}\right) - t_{\mathrm{trigger}} \tag{10}$$

4.2.4. Mechanical Activity and Parasitic Overhead

The mechanical effort demanded by the dual-axis stage is quantified by summing discrete motor microstep displacements along the zenithal (S_{el}) and azimuthal (S_{az}) axes:

$$S_{\mathrm{el}} = \sum_{k=1}^{N}|X_k - X_{k-1}|, \quad S_{\mathrm{az}} = \sum_{k=1}^{N}|Y_k - Y_{k-1}| \tag{11}$$

$$S_{\text{tot}} = S_{\text{el}} + S_{\text{az}} \tag{12}$$

Furthermore, the Parasitic Consumption Ratio (PCR) evaluates the net energetic balance by comparing the energy consumed by the MCU board and NEMA 11 actuators ($E_{\text{parasitic}}$) against gross generated energy (E):

$$\text{PCR} = \frac{E_{\text{parasitic}}}{E} \times 100\% \tag{13}$$

To estimate the motion contribution without continuous supply telemetry, the measured active electrical powers are $P_X \simeq 1.2$ W and $P_Y \simeq 2.5$ W. For either axis, a commanded displacement of 60,000 steps takes approximately 10 s under the bench conditions, corresponding to $v_X \simeq v_Y \simeq$ 6000 steps/s. The implied movement-energy costs are

$$q_X = \frac{P_X}{v_X} \simeq 2.00 \times 10^{-4}\ \text{J/step}, \qquad q_Y = \frac{P_Y}{v_Y} \simeq 4.17 \times 10^{-4}\ \text{J/step}. \tag{14}$$

Thus, for absolute travelled step counts S_X and S_Y,

$$E_{\text{move}}\ [\text{Wh}] \simeq \frac{q_X S_X + q_Y S_Y}{3600} = 5.56 \times 10^{-8} S_X + 1.157 \times 10^{-7} S_Y. \tag{15}$$

Here a step means the same commanded increment as in the 60,000-step timing test, not necessarily a full rotor step or an internally interpolated driver microstep. The travel must sum absolute displacements, not signed net endpoint changes: outward and return perturbations both consume energy. Coordinate differences reconstructed from sparse logs may miss reversals between samples, whereas a cumulative movement counter must be checked for its coverage and reset at reboot before differencing.

Equation (15) is a first-order estimate of electrical energy during motion at the measured operating conditions, not a measurement of mechanical dissipation or total system consumption. It assumes that the measured mean travel speed and active power remain representative for tracking moves; acceleration, short-move overhead, driver settings, load and speed changes can alter the cost per step. A complete parasitic budget additionally requires the energy of the control electronics and any motor/driver holding or idle consumption, without double-counting contributions already included in the active-power measurements. Consequently, a total PCR cannot be inferred from step travel alone.

4.3. Selected Midday Evaluation on 30 October 2026

The October record is examined primarily over the selected 12:00–14:00 interval (`noon`), after the logged F5 correction update and before the later degraded tracking period. This is deliberately a favourable operating window, not a full-day performance claim. The retained coordinate samples span 12:00:01–13:59:56, giving 7195 s of coverage and 1440 samples at approximately 5-s intervals. There are no inter-sample gaps exceeding 15 s. The log contains parameter updates during this interval, including the adaptive threshold and filtering settings; this is therefore an operating-window characterization, not a fixed-parameter autonomous benchmark. The October data are analyzed with their own calibration and definitions rather than pooled with the September energy metrics.

On-target occupancy and spatial coverage. The window reaches $f_{\mathrm{on}} = 88.5\%$ (1275 of 1440 samples) under Eq. (9), with a peak short-circuit current of approximately 333 mA and peak pyranometer irradiance of approximately 1086 W/m^2. Figure 3 shows the measured current and irradiance together with on-target occupancy in 15-min bins. The occupancy approaches unity in the central part of the window but is lower near its ends, and brief current reductions remain visible. Thus, the result supports sustained high-current operation during the selected interval without implying uninterrupted focal alignment or a measured energy efficiency of 88.5%.

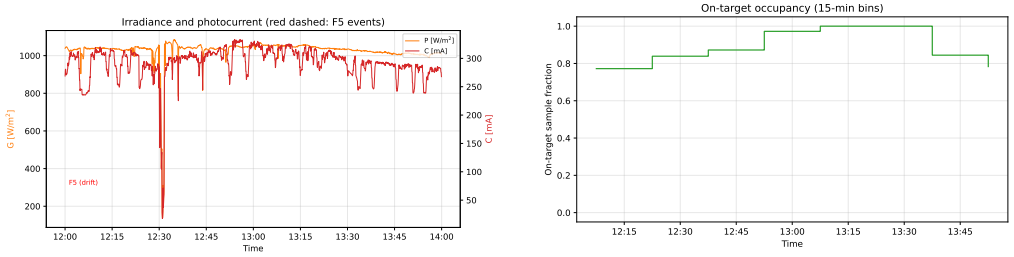


Figure 3: Selected panels from the 30 October 2026 midday tracking figure. Left: calibrated irradiance and short-circuit current. Right: fraction of samples satisfying the illuminated 80%-of-window-peak current criterion in successive 15-min bins (shown on a 0–1 scale). The full-window sample occupancy is 88.5%; no F5 drift-correction event was logged within this interval.

Figure 4 complements the time series by displaying the maximum sampled current and irradiance in each visited coordinate bin. The 1440 samples occupy 1362 distinct (X, Y) coordinates and form a narrow band in stage space. Because this map combines sequential measurements under changing solar conditions, it is a sampled operating-trajectory map, not a simultaneous optical response scan. In particular, the normalized overlap marker in the original figure is a visualization of the binned signals, not an independently measured solar position or angular pointing error.

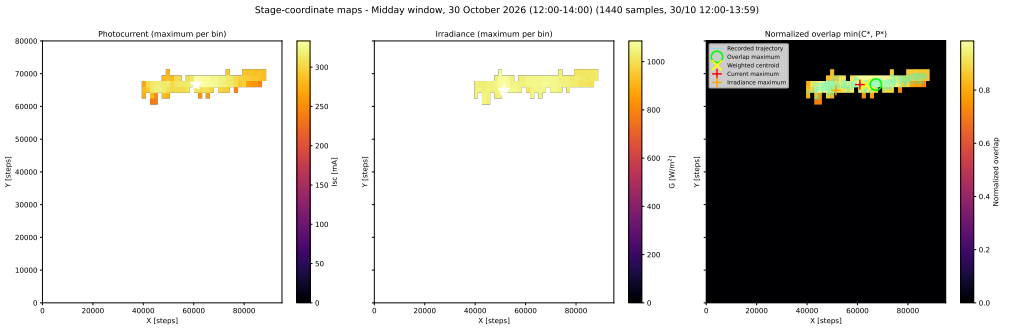


Figure 4: Midday stage-coordinate maps on 30 October 2026: maximum short-circuit current per visited bin (left), maximum pyranometer irradiance assigned to the corresponding sampled coordinates (centre), and normalized signal overlap with the recorded trajectory (right). Unvisited bins do not establish off-target optical behaviour, and the pyranometer map does not represent a receiver-position-dependent irradiance measurement.

Movement-energy estimate. The cumulative-counter trace and its interval rate are shown in Fig. 5. The first and last retained telemetry samples occur at 12:00:02 and 13:59:52, with post-

Table 1: Tracking and motion indicators for the selected 30 October 2026 midday window. The `TEL` increment counts commanded fine-tune steps; sampled axis travel sums absolute coordinate differences, not net endpoint displacement.

Indicator	Value
Coordinate-sample interval	12:00:01–13:59:56
Samples / distinct coordinates	1440 / 1362
On-target sample fraction f_{on}	88.5%
Peak I_{sc} / peak G_{POA}	333 mA / 1086 W/m^2
Cumulative-counter increment	773,235 steps
Sampled travel S_X / S_Y	386,277 / 387,658 steps
Sampled-travel movement estimate	0.0663 Wh
Counter increment per coordinate-window minute	6448.1 steps/min
Sampled direction reversals, X / Y	298 / 244
Logged F5 events / gaps exceeding 15 s	0 / 0

reboot counter values of 109,109 and 882,344 steps, giving an increment of 773,235 steps. Inspection of the firmware shows that this counter accumulates absolute commanded fine-tune increments from both axes, rather than all actuator motion: separate positioning, F5 corrections and homing are not included, and the counter resets at reboot. No F5 event or homing command is logged within the selected window, and the counter shows no reset there; absence from these logs is not an independent measurement of zero uncounted motion. The sampled coordinates also show 298 direction reversals in X and 244 in Y. High on-target occupancy therefore does not by itself establish negligible hunting or a low total parasitic budget.

For an axis-resolved estimate, summing absolute differences between the 1440 coordinate samples gives $S_X = 386{,}277$ and $S_Y = 387{,}658$ steps. Their sum is 773,935 steps, 700 above the retained `TEL` increment. The initial 700-step Y move after the first coordinate sample is already included in the first cumulative telemetry reading and therefore cancels when differencing the telemetry endpoints. Thus the two calculations have different temporal boundaries, rather than being interchangeable totals. Applying Eq. (15) to the sampled travel yields

$$E_X \simeq 77.26\ \text{J} = 0.02146\ \text{Wh}, \qquad E_Y \simeq 161.52\ \text{J} = 0.04487\ \text{Wh}, \tag{16}$$

$$E_{\text{move,sampled}} \simeq 238.78\ \text{J} = 0.06633\ \text{Wh}, \qquad \overline{P}_{\text{move,sampled}} \simeq 33.2\ \text{mW}. \tag{17}$$

The average is taken over the entire 7195-s coordinate window, not just the time in motion. This is an estimate based on sampled travel and bench conditions; any outward-and-return motion between coordinate samples remains unresolved.

If the logged increment is represented as an axis-partitioned total $S_X + S_Y = 773{,}235$, the unequal axis costs in Eq. (14) give the conditional range

$$E_{\text{move,counted}} \simeq 0.0430\text{–}0.0895\ \text{Wh} \quad (154.6\text{–}322.2\ \text{J}). \tag{18}$$

The lower endpoint assigns all counted steps to X, and the upper endpoint assigns them to Y; neither assignment is asserted to describe the actual trajectory. These are allocation bounds within the constant-power, constant-speed model, not uncertainty limits on Eq. (17) or bounds on total system consumption. An axis-resolved pulse counter covering every movement would avoid relying on sparse-coordinate reconstruction, and movement omitted by `TEL` would have to

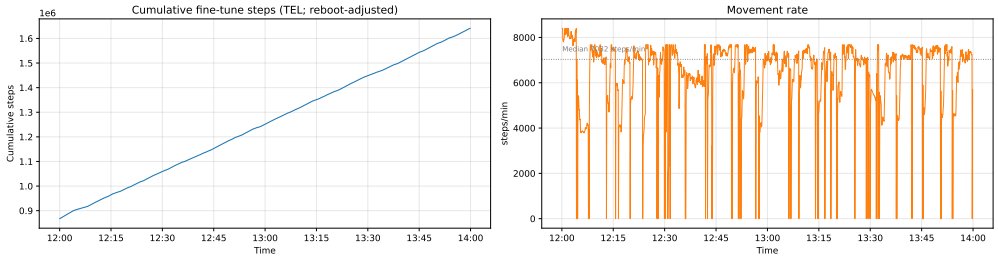


Figure 5: Motion panels from the original midday `energy` figure: cumulative logged step count (left) and interval movement rate (right). These panels show motion activity rather than measured electrical energy. The vertical offset in the cumulative counter includes earlier motion and is removed when computing the window increment.

be added separately. A net harvested-energy value and total PCR are therefore not claimed for this window. The model nevertheless makes the controller trade-off explicit: suppressing one unnecessary Y-axis step saves approximately 2.08 times the movement energy of suppressing one unnecessary X-axis step under the measured conditions.

4.4. Cross-Day Comparison of the Outdoor Sessions

A single measurement day cannot by itself establish that the reported tracking behaviour is representative rather than an artefact of a particular sky. We therefore repeated the outdoor campaign on a second, meteorologically distinct day and compared each session against its own reference focal ceiling P_{ref} (Eq. (6)), isolating the effect of the irradiation conditions from the controller (Fig. 6, Table 2). The 14 September 2025 session (capture B) ran from 10:28 to 14:57 and was markedly cloudier and lower in irradiance than the 21 September session (10:40–17:49): its accumulated plane-of-array irradiation was 2.93 kWh/m^2 against 3.33 kWh/m^2, with ten cloud transients (up to 79% depth) against five, and a larger share of the record clipped at the pyranometer full scale.

Table 2 reports the headline metrics (full-session window, $G > 50$ W/m^2) for the two days. The 21 September session reached a tracking efficiency of 67.3% with a mean absolute power error of 72.4 mW; on the cloudier 14 September session the efficiency dropped to 52.3% and the error rose to 136.7 mW, while the normalized yield E/H stayed in the same band (0.230 vs 0.278 Wh per kWh/m^2). This efficiency drop tracks the irradiation deficit and the higher cloud loading rather than any change in controller behaviour: the adaptive fine-tune threshold converged to the same aggressive value ($e = 800\,\mu$steps) on both days, and the steady-state offset of the tracked peak with respect to the astronomical target was actually smaller on 14 September (0.4°/2.7°) than on 21 September (2.5°/4.9°). Mechanical activity remained of the same order (1.5×10^6 vs 3.3×10^6 μsteps over 2228° vs 4956° of axis travel). The two sessions thus mutually corroborate the controller: under substantially different sky conditions it reproduces the same operating regime and keeps the harvested power locked to the moving focal ceiling.

4.5. Detailed Evaluation of the 21 September Session

Section 4.4 compared the two outdoor sessions at the headline level. This subsection now examines, in detail, the most complete record of the campaign, carried out on 21 September 2025 (local time, UTC-6) in Aguascalientes, Mexico. The dual-axis stage operated in the solar-tracking state from 10:42:24 to 17:02:34 (6.34 h), logging 11,174 samples at approximately

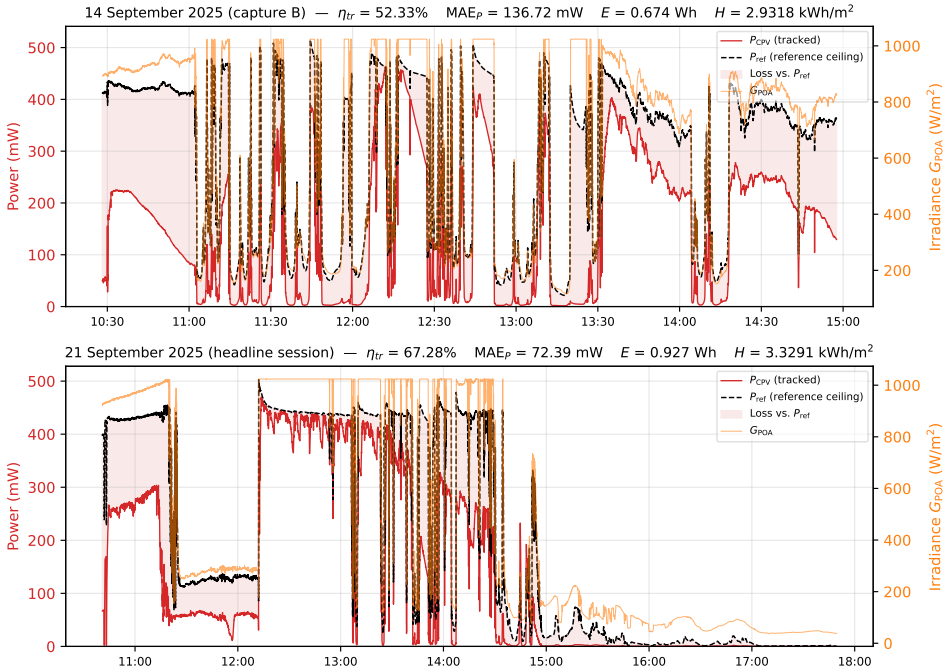


Figure 6: Cross-day comparison of the harvested power P_{CPV} (red) against the per-session reference focal ceiling P_{ref} (black dashed) and the plane-of-array irradiance G_{POA} (orange, right axis). Top: 14 September 2025 (capture B); bottom: 21 September 2025 (headline session). In both days P_{CPV} tracks the irradiance-driven ceiling through the cloud transients without losing lock; the shaded region is the instantaneous loss with respect to P_{ref}.

Table 2: Cross-day headline metrics (full-session window, $G > 50$ W/m^2). Each session is referenced to its own P_{ref} ceiling (Eq. (6)).

Day (2025)	E (Wh)	H (kWh/m^2)	E/H (Wh/kWh m^{-2})	η_{tr} (%)	MAE$_P$ (mW)
14 Sep	0.67	2.93	0.230	52.3	136.7
21 Sep	0.93	3.33	0.278	67.3	72.4

10 samples/s. The day was partially cloudy: plane-of-array irradiance G ranged from 37 to 1024 W/m^2, 69.7% of the daylight samples ($G > 200$ W/m^2, 4.64 h in total) exceeded 600 W/m^2, a prolonged cloud interval between 11:20 and 12:05 reduced G from 971 W/m^2 to a minimum of 153 W/m^2 (−84%), and five short cloud transients (36.6–87.4% depth) occurred between 13:41 and 16:01. Throughout the illuminated period the micro-CPV cell voltage stayed in the 2.32–2.62 V range and the short-circuit current in the 0.136–0.234 A range, confirming the sanity of the electrical measurements used below.

Energy balance and tracking efficiency. Table 3 summarizes the energy balance and the tracking efficiency for the evaluation windows defined in Sec. 4.2. The full-session row spans a contiguous record and is the headline result of the day: the prototype generated $E = 0.93$ Wh against a plane-of-array irradiation of $H = 3.33$ kWh/m^2, i.e. a normalized yield of $E/H = 0.278$ Wh per kWh/m^2, with a tracking efficiency of 67.3%. The subset rows are computed over non-contiguous samples (the gaps are bridged by the trapezoidal integration), so their absolute E and H values should be read as upper bounds.

Table 3: Energy and tracking metrics, measurement session of 21 September 2025 (Aguascalientes, Mexico, UTC-6).

Window	E (Wh)	H (kWh/m^2)	E/H (Wh/kWh m^{-2})	η_{tr} (%)	MAE$_P$ (mW)
Full session ($G > 50$ W/m^2)	0.93	3.329	0.278	67.3	72.4
Daylight ($G > 200$ W/m^2)	0.94	3.257	0.290	67.6	105.4
Tracking active (status=3)	0.93	3.307	0.280	67.6	71.7

Fig. 7 shows the measured CPV power P_{CPV} against the reference ceiling P_{ref} (Eq. (6)) and the irradiance for the whole session. The two curves follow one another closely through the morning cloud interval and the five afternoon transients, and the controller never loses lock: P_{CPV} reproduces the shape of the irradiance profile, including the deepest transients, without drops to zero. Restricted to the direct-sky intervals ($G > 600$ W/m^2), the median power ratio $P_{\mathrm{CPV}}/P_{\mathrm{ref}}$ is 0.73 and only 22% of the samples reach 95% of P_{ref}. This residual offset is attributed to the angular-response mismatch between the flat pyranometric sensor that defines P_{ref} and the concentrating optics of the micro-CPV cell (Eq. (6)); it is an intrinsic property of the reference definition rather than a controller failure.

Position with respect to the astronomical target. Fig. 8 compares the camera-estimated stage position with the astronomical target computed from the solar coordinates. The target is essentially fixed on the stage frame over the short recentering windows (the apparent solar motion is slow), whereas the camera tracks the electrical peak. After each recentering command the per-axis error converges in 5–10 min to a steady offset of 2.3–2.6° on the azimuthal axis (X) and 4.2–4.9° on the zenithal axis (Y) of stage travel. The recentering issued at 10:42:23 left an initial X offset of 0.15° and the one at 10:43:29 of 1.21°. The persistent, larger Y offset is consistent with the sensor/optics mismatch discussed above: the camera systematically locks onto an electrical peak displaced from the geometric aim point.

Disturbance recovery. The three recovery triggers logged that morning (two *Track-solar* and one *Recentering* commands) fired before sunrise, while the stage was parked in the dark ($P_{\mathrm{min}} = 2.2$ mW; Fig. 9). No t_{95} crossing occurred within the 20-min evaluation window; the power first crossed 95% of P_{ref} 5328–5397 s (89–90 min) after the trigger, i.e. only once the Sun rose. The

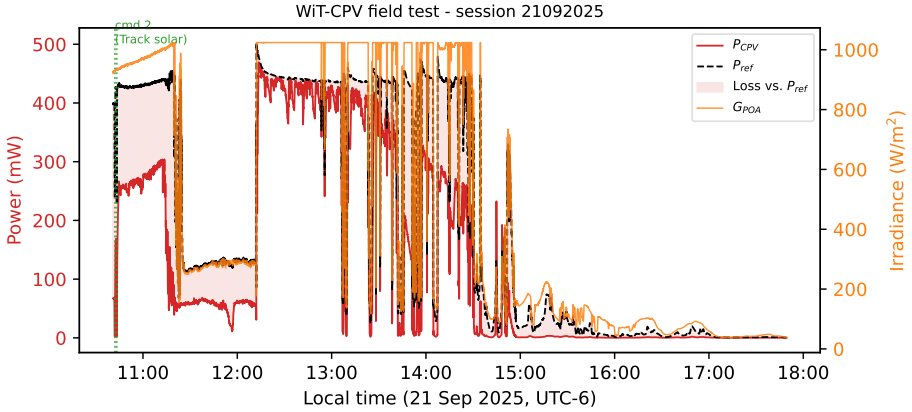


Figure 7: Measured CPV power P_{CPV} (red) against the reference ceiling P_{ref} (black) and the plane-of-array irradiance (orange, right axis), 21 September 2025 (10:40–17:49 UTC-6). The 11:20–12:05 cloud interval and the afternoon transients reduced the irradiance by up to 87%; the dotted vertical line marks the start of the track-solar command.

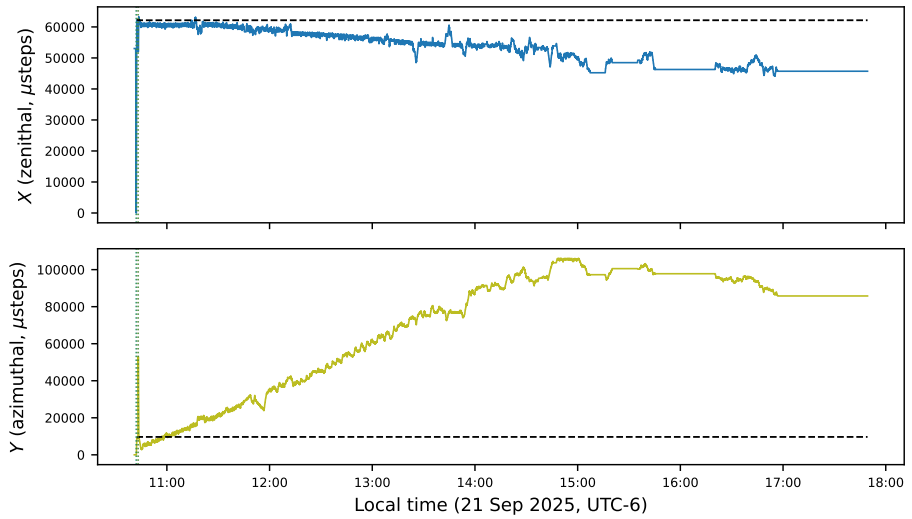


Figure 8: Top: camera-estimated position (red) versus astronomical target (blue) in the stage coordinate frame (X: azimuthal axis, Y: zenithal axis, in degrees of axis travel); the two recentering commands are marked. Bottom: per-axis error; after each recentering the error converges to a steady offset of ≈2.5° (X) and ≈4–5° (Y).

informative recovery measurements of the day are therefore the cloud transients: Table 4 lists the five events detected by the criterion of Sec. 4.2. The two deep transients (87% depth, G down to 125–133 W/m^2) recovered to 95% of their pre-event irradiance in 170–180 s, and P_{CPV} recovered in the same time order (Fig. 7), indicating that the controller re-acquires the peak within a few minutes after each transient.

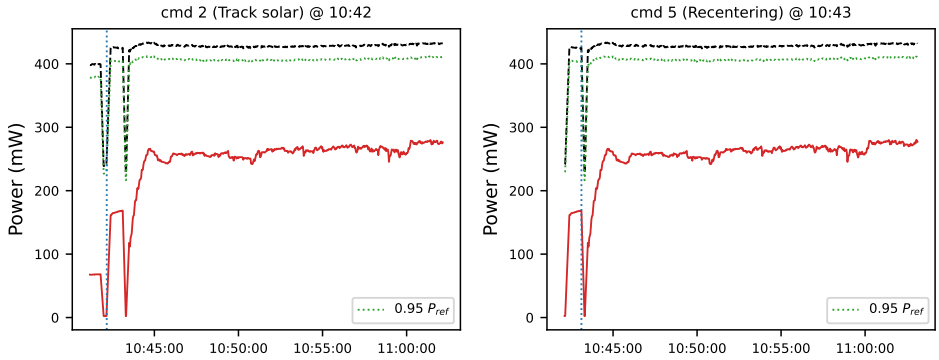


Figure 9: Recovery windows around the pre-sunrise triggers (10:42:10 and 10:43:07): P_{CPV} (red) versus P_{ref} (black dashed) and the 95% threshold (green dotted). No t_{95} crossing occurs within the 20-min window because the triggers fired before sunrise; the first crossing happens 89–90 min later.

Table 4: Cloud transients detected on 21 September 2025 and irradiance recovery time t_{95}^{G} (time for G to return to 95% of the pre-event baseline).

t_{start} (HH:MM:SS)	$G_{\mathrm{base}} \rightarrow G_{\mathrm{min}}$ (W/m^2)	Depth (%)	Duration (s)	t_{95}^{G} (s)
13:41:55	989 → 125	87.4	178	180
14:04:37	1024 → 133	87.0	166	170
15:06:55	148 → 80	46.1	132	136
15:47:11	103 → 58	43.8	120	124
15:59:53	70 → 44	36.6	154	160

Adaptive fine-tune threshold and mechanical activity. Fig. 10 shows the evolution of the adaptive fine-tune threshold e (Eq. 1): it dropped from 1500 to 800 usteps between 10:41 and 10:43 and remained constant for the rest of the session, while the error signal settled on a plateau of the order of 10^3 usteps. The auto-tune (AT) snapshot taken at 13:56:04 recommended thresholds of 2844 usteps (small), 53,443 usteps (abrupt) and 196,226 usteps (reset), with a peak proximity of 0.01. The operating threshold (800 usteps) therefore ran about 3.5× below the AT-recommended lower bound all day, i.e. the controller operated in a more aggressive regime than the one proposed by the auto-tuner. This is consistent with the mechanical activity logged by the encoders: $S_{\mathrm{el}} = 1.61 \times 10^6$, $S_{\mathrm{az}} = 1.62 \times 10^6$ and $S_{\mathrm{tot}} = 3.23 \times 10^6$ usteps, equivalent to 4876° of total axis travel in 6.34 h (≈12.8°/min on average).

Parasitic overhead. The parasitic consumption ratio (Eq. 13) could not be evaluated for this session because the power supply did not log the board and motor consumption. The later axis-

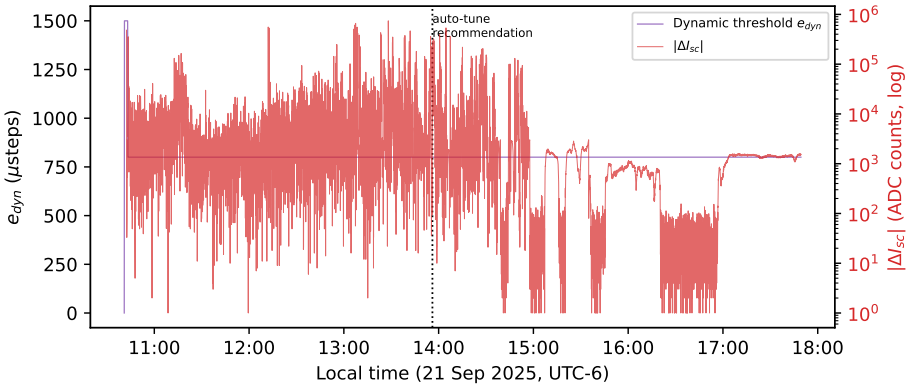


Figure 10: Adaptive fine-tune threshold e (blue, left axis) and the fine-tune error signal (red, right axis, log scale) during the session. e dropped from 1500 to 800 usteps at 10:43 and then stayed constant; the vertical dashed line marks the 13:56:04 auto-tune snapshot, which recommended a lower bound of 2844 usteps, about 3.5× above the 800 usteps threshold actually in use.

power measurements enable the conditional motion estimate in Sec. 4.3, but are not retroactively applied to the September hardware and settings. A complete $E_{\text{parasitic}}$ still requires supply telemetry.

5. Conclusions

The selected midday record of 30 October 2026 adds a well-defined favourable operating case: 88.5% of 1440 samples met the illuminated 80%-of-window-peak current criterion between 12:00:01 and 13:59:56, with no logged F5 correction event. This occupancy is not directly comparable with energy-based tracking efficiency or representative of the entire day, and the window includes parameter adjustments. Bench powers of 1.2 W (X) and 2.5 W (Y), together with approximately 10 s per 60,000 steps, yield movement costs of 0.200 and 0.417 mJ/step. Applied to the sampled axis travel, these give 0.0663 Wh (238.8 J) of estimated movement energy, equivalent to 33.2 mW averaged over the window. The separate fine-tune-counter increment of 773,235 steps gives an axis-allocation range of 0.0430–0.0895 Wh for counted motion. Neither calculation includes unobserved travel, holding or controller consumption. The result establishes a first-order way to connect search activity to parasitic energy, not a measurement of total net yield or PCR.

This work presented a step-adaptive Perturb and Observe control strategy and its embedded implementation for the tracking-integrated WiT-CPV prototype, in which the multi-junction cell is kept on the moving Petzval focal spot by I_{sc}-based feedback without an active MPPT stage. The four-regime structure (static hold, near-peak fine convergence, cloud-transient shielding, and search re-initialization) suppressed mechanical hunting under steady irradiance while remaining responsive to fast sky transients, and the dual-core ESP32 board with TMC2209 stepper drivers, sensorless StallGuard4 homing, and a 24-bit delta-sigma ADC provided the synchronized I_{sc}/V_{oc} sensing and IoT telemetry required by the closed loop.

Quantitatively, over the outdoor session of 21 September 2025 the controller harvested E = 0.93 Wh against a plane-of-array irradiation of H = 3.33 kWh/m^2 (E/H = 0.278 Wh per

kWh/m^2), with a tracking efficiency of 67.3% and a mean absolute power error of 72.4 mW for the full session (67.6% and 71.7 mW over the tracking-active window). The stage accumulated 3.23×10^6 microsteps (≈4876° of axis travel in 6.34 h), and the adaptive fine-tune threshold settled at 800 usteps, about 3.5× below the lower bound recommended by the in-session auto-tuner, i.e. the loop operated in a more aggressive regime than the one proposed by the auto-tune routine. The pre-sunrise recentering triggers yielded no t_{95} crossing within the 20-min evaluation window (the first crossing occurred only at sunrise, 89–90 min later), so the informative recovery measurements were the five afternoon cloud transients: the irradiance returned to 95% of its pre-event baseline in 124–180 s for the two deepest events (87% depth), and P_{CPV} re-acquired the peak within the same time frame, confirming that the shielding and re-initialization regimes work as designed under real sky conditions. A cross-day check against a second, cloudier session (14 September 2025, Sec. 4.4) confirmed that these figures are representative rather than day-specific: the loop converged to the same fine-tune threshold and a comparable angular offset, with the tracking efficiency scaling from 67.3% to 52.3% in proportion to the reduced irradiation and higher cloud loading.

Three limitations were identified. First, a persistent steady offset of ≈2.5° (azimuthal axis) and 4–5° (zenithal axis) with respect to the astronomical target remained after each recentering, which is attributed to the angular-response mismatch between the flat pyranometric reference sensor and the concentrating optics rather than to a controller fault. Second, the parasitic consumption ratio could not be quantified in this session because the board and motor consumption was not logged; it will be reported once the supply telemetry is available. Third, the plane-of-array pyranometer saturates at its full scale of 1024 W/m^2, so the midday irradiance (42.6% of the daylight samples, ≈100 min) is clipped at that value. A clear-sky curve $G_{\mathrm{cs}} = A\, e^{-B\,\mathrm{AM}} + C$ calibrated on the unclipped intervals of the same session places the true peak irradiance at ≈1036 W/m^2; the clipping therefore keeps the reported H and η_{tr} slightly low (by 0.4% in H and 0.5 percentage points in η_{tr}), so the quantitative conclusions are unaffected.

As future work, the dual-layer hybrid scheme of Sec. 3.3, which couples open-loop astronomical positioning with the closed-loop fine alignment to eliminate search delays under heavy cloud cover, will be implemented on the prototype. The next outdoor iterations will add board-consumption logging to quantify the PCR, refine the fine-tune threshold scheduling against the auto-tuner recommendations, and characterize the steady angular offset against a goniometric reference to separate its optical from its mechanical contributions.

References

[1] Grażyna Frydrychowicz-Jastrzębska and Artur Bugała. “The influence of external conditions and orientation of PV module on the energetic gain”. In: *Computer Applications in Electrical Engineering* 11 (2013), pp. 423–439.

[2] AL-Rousan Nadia, Nor Ashidi Mat Isa, and Mohd Khairunaz Mat Desa. “Advances in solar photovoltaic tracking systems: A review”. In: *Renewable and sustainable energy reviews* 82 (2018), pp. 2548–2569.

[3] Hossein Mousazadeh et al. “A review of principle and sun-tracking methods for maximizing solar systems output”. In: *Renewable and sustainable energy reviews* 13.8 (2009), pp. 1800–1818.

[4] AZ Hafez, AM Yousef, and NM Harag. "Solar tracking systems: Technologies and trackers drive types–A review". In: *Renewable and Sustainable Energy Reviews* 91 (2018), pp. 754–782.

[5] Anshul Awasthi et al. "Review on sun tracking technology in solar PV system". In: *Energy Reports* 6 (2020), pp. 392–405.

[6] Reza Sadeghi et al. "A review and comparative analysis of solar tracking systems". In: *Energies* 18.10 (2025), p. 2553.

[7] Rosa F Fuentes-Morales et al. "Control algorithms applied to active solar tracking systems: A review". In: *Solar Energy* 212 (2020), pp. 203–219.

[8] Vijayan Sumathi et al. "Solar tracking methods to maximize PV system output–A review of the methods adopted in recent decade". In: *Renewable and Sustainable Energy Reviews* 74 (2017), pp. 130–138.

[9] Andrea Antonini. "Photovoltaic Concentrators-Fundamentals, Applications, Market & Prospective". In: *Sol. Collect. Panels, Theory Appl., Sciyo* (2010), pp. 31–54.

[10] Waseem Iqbal, Irfan Ullah, and Seoyong Shin. "Optical developments in concentrator photovoltaic systems—a review". In: *Sustainability* 15.13 (2023), p. 10554.

[11] Maria A Ceballos et al. "Tracking-integrated cpv technology: State-of-the-art and classification". In: (2023).

[12] Marthoz Angulo-Calderón et al. "Development and accuracy assessment of a high-precision dual-axis pre-commercial solar tracker for concentrating photovoltaic modules". In: *Applied Sciences* 12.5 (2022), p. 2625.

[13] Atsushi Ito, Daisuke Sato, and Noboru Yamada. "Optical design and demonstration of microtracking CPV module with bi-convex aspheric lens array". In: *Optics Express* 26.18 (2018), A879–A891.

[14] S Askins et al. "Performance of hybrid micro-concentrator module with integrated planar tracking and diffuse light collection". In: *2019 IEEE 46th Photovoltaic Specialists Conference (PVSC)*. IEEE. 2019, pp. 2507–2512.

[15] Kareem Younes et al. "Realizing high photovoltaic power densities with tracking-integrated concentrator photovoltaics". In: *Frontiers in Energy Research* 10 (2022), p. 842201.

[16] Santiago Maestro, D Chemisana, and Hasan Baig. "Fabrication and experimental validation of a building-integrated microtracking CPV system". In: *Renewable Energy* (2025), p. 124508.

[17] Arturo Díaz-Ponce et al. "Development of a proof-of-concept concentrating photovoltaic module with integrated tracking and azimuthal cell rotation". In: *Results in Engineering* 27 (2025), p. 106735. DOI: 10.1016/j.rineng.2025.106735.